Analysis of a Complementary Dual-Stator Vernier Machine with Reduced Non-Working Harmonics for Low-Speed Direct-Drive Applications

Jiahui Huang, Weinong Fu, Shuangxia Niu*, *Senior Member, IEEE*, and Xing Zhao, *Member, IEEE*

***Abstract*—This paper presents a comprehensive analysis of a novel complementary dual-stator Vernier machine (DSVM) with improved performance. In contrast to conventional DSVMs, the proposed machine employs a unique configuration featured by a complementary stator design alongside phase-shifted dual stator winding. Therefore, the symmetry of flux distribution is improved, and the non-working even order harmonics produced by the armature winding are effectively reduced. Consequently, the power factor is notably improved to 0.91, and the unbalanced force is reduced by 60.14% compared to the conventional DSVM. The electromagnetic performance, mechanical structure and thermal analysis are well investigated by using finite element analysis (FEA). In addition, the temperature rise under the rated load condition with natural cooling is safe, and the mechanical strength is proved to be sufficient, which validates the feasibility of the proposed novel design. Finally, a prototype is fabricated, and the performance is tested to verify the feasibility of the proposed design.**

***Index Terms*—Dual-stator Vernier machine, flux-modulation, power factor, unbalanced magnetic force, thermal analysis.**

I. INTRODUCTION

THE direct-drive systems are currently widely used in various applications like electric vehicles, elevators, ships, and renewable energy conversion systems. Vernier machines (VMs) are considered a robust solution for various low-speed applications [1], [2]. With ongoing research, the torque and power density of VMs have been further improved by incorporating permanent magnets (PMs) onto the rotor, as demonstrated in [3]. The permanent magnet Vernier machine (PMVM), which combines the advantages of both Vernier and PM machines, exhibits high torque density and efficiency at a low rotational speed [3], [4]. Therefore, it has become a promising candidate for low-speed direct-drive systems.

Several topologies have been well-studied to further improve the electromagnetic performance of PMVMs [5]-[10]. References [5] and [6] illustrated the working principle of the PMVM from the perspective of the flux modulation effect. References [7] and [8] comparatively analyzed several PMVMs with concentrated windings. In [9], a novel concentrated winding multi-working harmonics PMVM with specially designed stator auxiliary teeth was proposed, resulting in a significant 20% increase in output torque compared to a conventional PMVM with a concentrated winding. In addition, a novel consequent-pole toroidal-winding outer rotor PMVM was introduced in [10] with both improved torque density and torque per magnet volume. Compared to the conventional PMVM, this design achieved a 20% higher output torque while using only 60% of magnets.

However, the improvement of single-stator single-rotor structures is limited. As torque and power density requirements continue to increase, the conventional structure of the PMVM may no longer be sufficient to meet these demands. In response, dual-stator structure Vernier machines (DSVMs) have been proposed, which effectively utilize the previously unused space within the machine structure and have the potential to further enhance torque density [11]-[17]. In [11], a DSVM with two sets of drum windings and surface-mounted PMs was introduced, with the adoption of key design components well-explained. Reference [12] presented an advanced spoke-type DSVM with a high output torque of 2000 Nm, while [13] compared different stator structures of the spoke-type DSVM. In [14], a comparison of Halbach single stator PMVM, yokeless PM DSVM, and spoke-type DSVM was made, with the spoke-type structure exhibiting the highest torque density. Reference [15] proposed a hybrid magnet DSVM that features magnets mounted on both outer and inner stators with reverse polarity. Although the aforementioned dual excitation DSVMs effectively enhance the torque density, they also face thermal issues in the inner stator, similar to those observed in regular dual-stator PM machines. To address this issue, a single-winding DSVM with an inner stator winding removed was proposed in [16]. Reference [17] comprehensively compared the performance of dual stator winding DSVM, single winding DSVM, and single stator single rotor structures. Apart from improving torque density, the dual-stator structure has also been found to enhance power factor and address the low power factor issue of Vernier machines [18]-[21]. For instance, in [18], a novel high torque density, high power factor spoke-type DSVM was proposed with a power factor of 0.85. Similarly, in [19], a yokeless DSVM was proposed that exhibits improved power factor and better overload capability. The effect of various parameters on the power factor was also studied. In [20], a consequent-pole DSVM with reduced magnet consumption and enhanced power factor was presented. Moreover, reference [21] investigated the optimal turn-number assignment of the inner

and outer stator windings to achieve a high power factor and provided guidelines accordingly.

This paper proposes a novel DSVM machine with reduced non-working harmonics armature winding design. This machine exhibits improved performance in power factor and unbalanced force. A comprehensive analysis, including electromagnetic, mechanical and thermal aspects, is presented in this paper. This paper is organized as follows: Section II explains the electromagnetic and mechanical structure of the proposed design, along with its working principle. Then, the performances, including torque, power factor, and unbalanced force, are analyzed in Section III. Mechanical strength and thermal verification are conducted in Section IV and Section V, respectively. Subsequently, a prototype is fabricated and tested to verify the simulated results in Section VI. Finally, the main findings of this study are concluded in Section VII.

II. Machine Structure and Working Principle

In this section, both electromagnetic design and mechanical structure design are presented. Meanwhile, the reasons for the performance improvement are revealed.

A. Electromagnetic Design

The structure of the proposed DSVM is shown in Fig. 1. The stator and rotor combination satisfies [22]

$$N_r = |N_s \pm P_a| \quad (1)$$

where N_r is the rotor PM pole-pair number, N_s is the number of flux modulators, and P_a is the pole-pair number of the armature winding. Unlike the conventional open slot structure, a split-teeth structure is adopted in the proposed DSVM. N_s equals the product of the stator slots numbers (N_{slot}) and split-tooth numbers. The main design parameters are listed in Table I.

TABLE I
Main Design Parameters of the Proposed DSVM

Parameters	Values
Number of stator slots	9
Number of rotor pole pairs	13
Number of split-tooth numbers	2
Stator outer diameter	200 mm
Stack length	75 mm
Air gap length	1 mm
Turns in series per phase	420
Current density	5A/mm^2
Rated current	7.8A
Rated speed	300 rpm
PM material	N38EH
Steel material	WG35WW300
Cooling method	Natural cooling

As shown in Fig. 1, the inner stator and outer stator have a relative position difference indicated by θ_0 (θ_0=20 deg.). The even-order harmonics can be effectively reduced with the inner stator winding shifted 180 mechanical degrees from the outer stator winding with an inverse connection. At the proposed position, the inner stator winding and outer stator winding can realize a 180-mechanical-degree shift. Consequently, the non-working even-order harmonics can be effectively reduced by this novel design. The winding connection is present in Fig. 2.

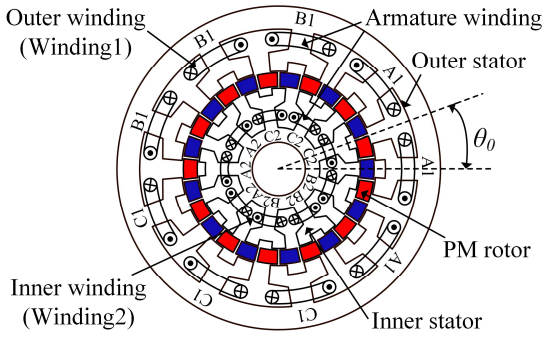

Fig. 1. Structure of the proposed DSVM.

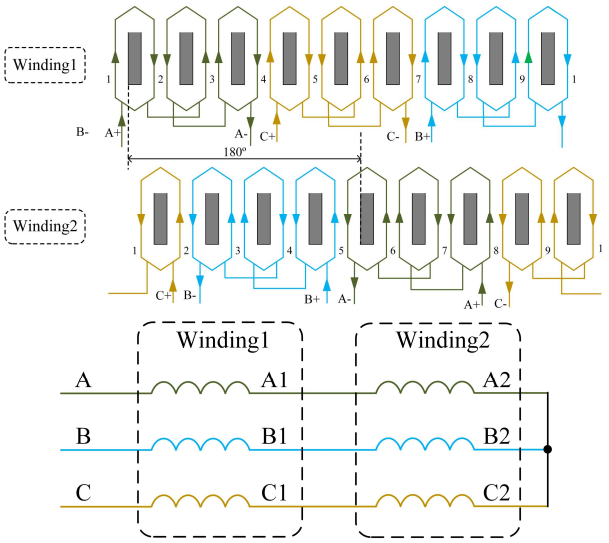

Fig. 2. Armature winding arrangement of the proposed DSVM.

B. Mechanical Structure Design

The overall structure that includes the mechanical mounting design is presented in Fig. 3. The proposed DSVM mainly consists of an outer stator, an inner stator, a rotor assembly, and auxiliary mounting components. An exploded view of the overall machine structure is shown in Fig. 3 (a). The outer stator is directly mounted onto the machine shell, providing stability and support for the motor. The inner rotor is securely fastened to a fixed shaft that extends from the rear end plate, ensuring precise alignment with the stator assemblies. The rotor assembly, which includes the PM rotor, is sandwiched between the inner and outer stators. The output shaft forms part of the rotor assembly and is supported by a bearing, which enables it to rotate smoothly and transmit output power.

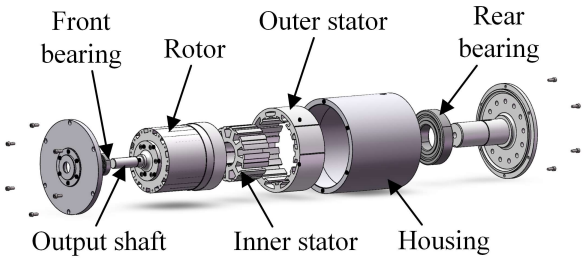

(a)

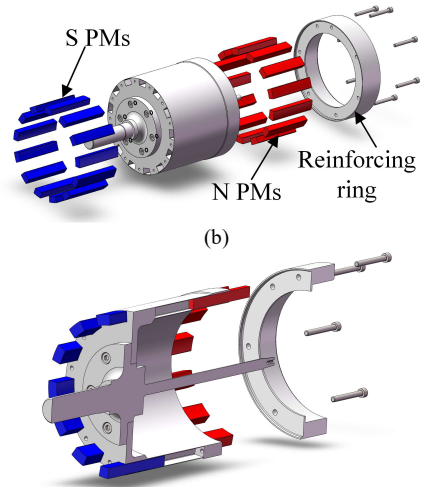

Fig. 3. Exploded view of the DSVM mechanical structure. (a) Overall structure. (b) Rotor structure. (c) Rotor cross-sectional view.

In order to provide a detailed illustration of the rotor assembly, Fig. 3 (b) and (c) show an exploded view and a cross-sectional view, respectively. The rotor assembly is a critical component of the dual-stator machine, responsible for generating the rotating magnetic field that interacts with the stator armature winding to produce torque. It consists of a stainless-steel rotor shell with PM segments inserted into cavities from different directions. The PMs with S polarity are inserted from the front side, while the PMs with N polarity are assembled from the rear side, creating an alternating magnetic field. The careful placement of the PM segments ensures proper alignment and balance, while the strict control of the surface thickness of the rotor shell maintains sufficient mechanical strength and accurate air gap thickness. Once the PM segments are in place, a reinforcing ring is assembled on the rear side of the rotor assembly. This ring provides additional support and stability, allowing the rotor to withstand high-speed rotation and heavy loads. The reinforcing ring is supported by a large bearing, which helps to distribute the load and reduce stress on the rotor components.

C. Reduction of Non-working Harmonics

Abundant harmonics are produced in the air gap due to the flux modulation effect in conventional VMs with fractional slot concentrated winding (FSCW) design. However, some non-working harmonics are also produced in addition to useful working harmonics. These extra non-working harmonics severely affect the performance of the VM.

The air gap flux density produced by the rotor PM can be obtained by

$$B_{pm}(\theta,t) = F_{pm}(\theta,t)\Lambda_s(\theta) \tag{2}$$

where F_{pm} is the magnetomotive force (MMF) of rotor PM and $\Lambda_s(\theta)$ is the permeance of both stators. F_{pm} is given by

$$F_{pm}(\theta,t) = \sum_{n=1}^{+\infty} F_n \cos[nN_r(\theta - \Omega_r t)] \tag{3}$$

where F_n is the amplitude of nth harmonic of MMF, Ω_r is the mechanical angular speed of the rotor.

Meanwhile, the air gap permeance can also be obtained by

$$\begin{aligned}\Lambda_s(\theta) = \frac{g}{\mu_0}\{&\Lambda_0\Lambda'_0 + \Lambda_0\sum_{k=1}^{+\infty}\Lambda'_k\cos(kN_s\theta+\theta_0) \\ &+\Lambda'_0\sum_{k=1}^{+\infty}\Lambda_k\cos(kN_s\theta) + \sum_{k=1}^{+\infty}\frac{\Lambda_k\Lambda'_k}{2}\cos[(2kN_s\theta)+\cos\theta_0]\}\end{aligned} \tag{4}$$

where Λ_0 and Λ_k are the average permeance value and the magnitude of the kth harmonic of the outer stator. Λ'_0 and Λ'_k refer to the corresponding values of the inner stator.

TABLE II
HARMONIC COMPONENTS OF NO-LOAD AIR GAP FLUX DENSITY

Group	Space harmonic order	Rotating speed
I	nN_r	Ω_r
II	$\lvert kN_s \pm nN_r\rvert$	$\frac{nN_r}{\lvert kN_s \pm nN_r\rvert}\Omega_r$
III	$\lvert 2kN_s - nN_r\rvert$	$\frac{nN_r}{\lvert 2kN_s - nN_r\rvert}\Omega_r$

According to (2)-(4), the air gap flux density excited by rotor PM can be deduced, and the harmonics are summarized in Table II.

The no-load phase back EMF can be obtained as

$$E_{ph}(t) = -\frac{d}{dt}[r_g l_{ef}\int_0^{2\pi} B_{pm}(\theta,t)N_a(\theta)d\theta] \tag{5}$$

where r_g is the radius of the air gap, l_{ef} represents the effective length of the motor, and $N_a(\theta)$ is the winding function.

Apparently, only the odd-order harmonics can be excited by the rotor PM. However, both even-order and odd-order harmonics exist in the conventional FSCW design apart from the main pole-pair harmonic that satisfies (1). In this study, the working harmonics of air gap flux density are in odd-order, which means that even-order harmonics are useless and even severely affect the performance of the proposed machine. Therefore, a special stator arrangement and advanced winding design are adopted in the proposed machine to reduce the non-working even-order harmonics produced by the armature winding. Different from the same inner and outer windings placement in the conventional DSVM, the inner and outer windings of the proposed machine have 180 degrees shifted (δ). In addition, the inner and outer windings are connected in series, and the polarity of the inner winding is inverted to achieve the effective superposition of the flux in the inner and outer windings. The MMFs of the inner and outer windings are shown in Fig. 4(a) and can be expressed as

$$F_{w1} = \frac{3}{2}\sum_{\substack{v=3k\pm1\\k=0,1,2...}}\frac{2\frac{N_t}{2}k_{wv}}{v\pi}I_m\cos(wt - v\theta) \tag{6}$$

$$F_{w2} = \frac{3}{2}\sum_{\substack{v=3k\pm1\\k=0,1,2...}}\frac{2\frac{N_t}{2}k_{wv}}{v\pi}[-I_m\cos(wt - v(\theta-\delta))] \tag{7}$$

where N_t is the number of turns of each phase, K_{wv} is the winding factor of vth harmonic, v is the winding MMF harmonic order, and I_m is the amplitude of the input current.

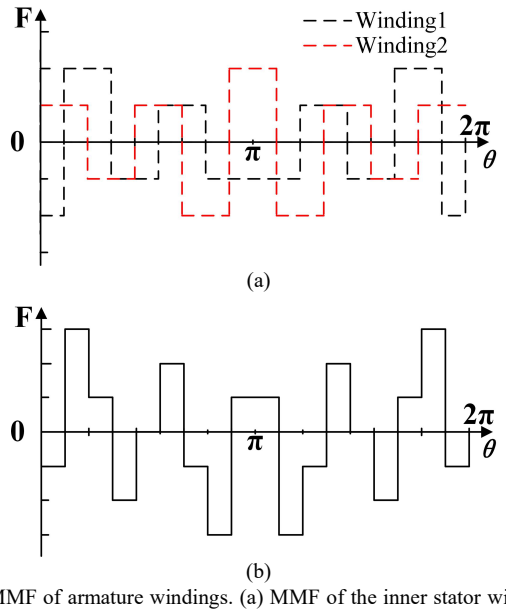

Fig. 4. MMF of armature windings. (a) MMF of the inner stator winding and outer stator winding. (b) Synthetic MMF.

Consequently, the synthetic MMF can be obtained as in (8), and the waveform is presented in Fig. 4(b).

$$F_w = F_{w1} + F_{w2} = \frac{3}{2}\sum_{\substack{v=6k\pm1 \\ k=0,1,2...}} \frac{2N_t k_{wv}}{v\pi} I_m \cos(wt - v\theta) \tag{8}$$

After applying the proposed winding design, the even-order harmonics have been eliminated, and only the odd-order working harmonics exist. The air gap flux density excited by the armature winding can be deduced and expressed as

$$B_w(\theta,t) = F_w \cdot \Lambda_s(\theta) \tag{9}$$

Hence, the even-order harmonics of air gap flux density produced by the armature winding are effectively eliminated. Furthermore, the flux linkage can be calculated as

$$\psi_a = r_g l_{ef} \int_0^{2\pi} B_w(\theta,t) N_a(\theta) d\theta \tag{10}$$

According to [23], the relationship between the power factor($\cos\varphi$) and inductance(L) can be defined as

$$\cos\varphi = \frac{1}{\sqrt{1+\left(\frac{\omega_e L I_s}{E_{\text{ph}}}\right)^2}} \tag{11}$$

where ω_e is the electrical angular speed, L is the inductance of the winding, and I_s presents the stator current. The inductance equals the sum of the armature reaction inductance and the leakage inductance. The leakage inductance is ignored in this study. Consequently, the inductance L can be derived by

$$L = \frac{\psi_a}{I_m} \tag{12}$$

Therefore, the inductance is reduced due to the reduction of the even-order harmonics in the armature reaction. As a result, the power factor is improved.

In addition, according to [24], [25], the radial force density can be expressed as

$$\sigma_r(\theta,t) = \frac{B_r^2(\theta,t)}{2\mu_0} \tag{13}$$

where $B_r(\theta,t)$ is the radial flux density, and it can be expressed as in (14) under the load condition. μ_0 is the permeability of the vacuum, θ is the mechanical angle along the circumference, and t is the time.

$$B_r(\theta,t) = B_{pm}(\theta,t) + B_w(\theta,t) \tag{14}$$

The radial force on the rotor can be obtained as

$$F_t(t) = F_x(t) + jF_y(t) = r_g l_{ef} \int_0^{2\pi} \sigma_r(\cos\theta + j\sin\theta) d\theta \tag{15}$$

Consequently, the relationship between the F_t and B_r can be expressed as

$$F_t \propto B_r^2 \tag{16}$$

Therefore, if the harmonics of the radial flux density can be effectively suppressed, it will play a positive role in weakening the unbalanced magnetic force of the machine. Equations (8) and (9) indicate that the non-working even-order harmonics produced by the armature winding are effectively mitigated. This results in the suppression of the harmonics of the radial air gap flux density, as per equation (14). Finite element analysis (FEA) further validates this suppression, as depicted in Fig. 5.

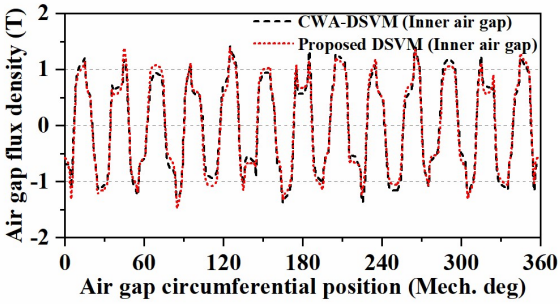

(a)

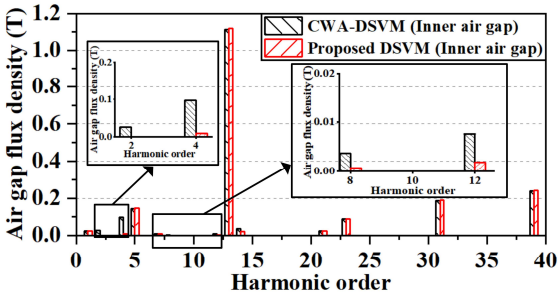

(b)

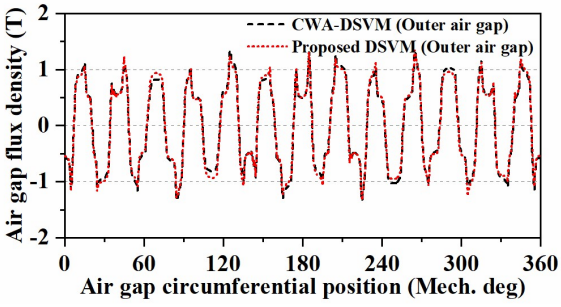

(c)

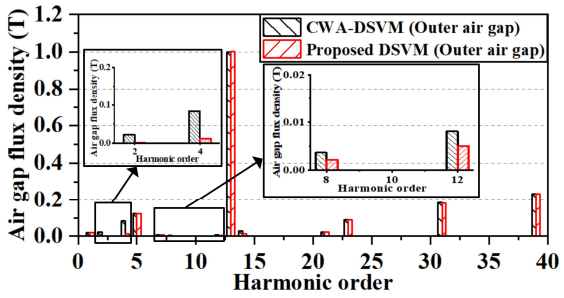

(d)

Fig. 5. On-load air gap flux density and spectra. (a) Waveforms of inner air gap flux density. (b) Spectra of inner air gap flux densities. (c)Waveforms of outer air gap flux density. (d) Spectra of outer air gap flux densities.

Fig. 5 compares the on-load air gap flux density and spectra of the DSVMs with both the conventional and proposed winding arrangements. In the conventional winding arrangement, the inner and outer windings are placed at the same position around the circumference of space. As shown in Fig. 5, the proposed arrangement reduces even-order space harmonics produced by the armature winding, mainly including 2^{nd}, 4^{th}, 8^{th}, and 12^{th}. Consequently, the unbalanced force of the proposed DSVM is effectively reduced compared to the DSVM with the conventional winding arrangement (CWA-DSVM).

The proposed machine utilizes a special method to improve the power factor and reduce the unbalanced force. The inner stator core is placed with a half-slot pitch position difference compared to the outer stator core, and the inner stator winding is mechanically shifted by 180 degrees compared to the outer stator winding. Not only the proposed machine in this paper but this method can also be applied to a variety of two split-tooth VMs that adopt the concentrated winding, which satisfies $N_s/2=2|N_s-N_r|\pm1$. The armature reaction MMF harmonics of even or odd orders (depending on which are the non-working harmonics) can be eliminated. The only difference between eliminating even or odd order harmonics is that, to eliminate even order harmonics, the polarity of the inner stator winding needs to be inverted.

III. Performance Investigation by FEA

In this section, the electromagnetic performance is analyzed after performing a global optimization of the proposed DSVM in terms of the output torque, power factor, and unbalanced magnetic force, are carried out. The optimized design parameters are listed in Table III.

A. Torque Performance

The phase back EMF of the proposed machine and its spectrum are shown in Fig. 6. The amplitude is 150.35 V at the rated speed of 300 rpm. It can be seen that the back EMF waveform is highly sinusoidal, which can be further explained by the low total harmonic distortion (THD) of the proposed machine. As shown in Fig. 6(b), only the 3^{rd} harmonic is non-negligible. However, the 3^{rd} harmonic can be ignored in the three-phase Y-connected machine. Consequently, The THD is only 0.41%.

TABLE III
THE STRUCTURAL DESIGN PARAMETERS OF THE PROPOSED DSVM

Parameters	Unit	Values
Stator outer diameter	mm	200
Stack length of iron core	mm	75
Air gap length	mm	1
Height of outer stator yoke	mm	8.1
Height of outer stator main tooth	mm	8.8
Width of outer stator main tooth	mm	23.9
Height of outer stator split tooth	mm	3.5
Arc of outer stator split teeth	deg.	11
Arc of outer stator dummy slot	deg.	9
Height of outer stator dummy slot	mm	4.6
Height of rotor PM	mm	10
Rotor PM pole-arc coefficient	/	0.9
Height of inner stator yoke	mm	11.9
Height of inner stator main tooth	mm	18.1
Width of inner stator main tooth	mm	13.4
Height of inner stator split tooth	mm	4.9
Arc of inner stator split teeth	deg.	11
Arc of inner stator dummy slot	deg.	9
Height of inner stator dummy slot	mm	2.5

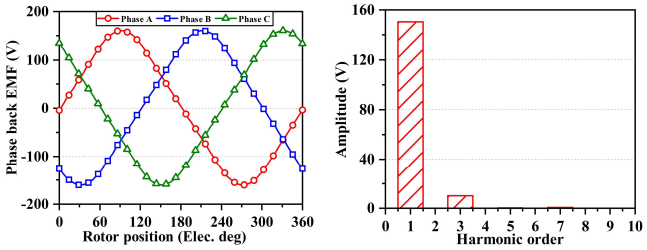

(a) (b)

Fig. 6. Phase back EMF of the proposed DSVM. (a) Waveforms. (b) Harmonic spectra.

Fig. 7 (a) shows the output torque of the proposed machine at the rated condition (with the current density of 5A/mm^2). The average torque is 78.34Nm. It can be found that the output torque is quite stable, and the torque ripple is as low as 0.61%. In addition, the proposed machine exhibits an excellent overload ability, as presented in Fig. 7 (b). It depicts the output torque of the proposed machine when the input current increases from 0 A to 15A (about 2 times the rated current). With the increment of the input current, the torque increases, and the curve shows good linearity.

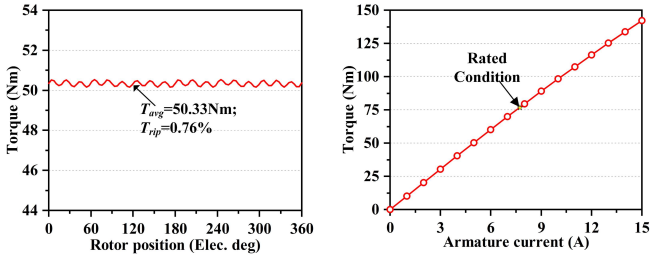

(a) (b)

Fig. 7. Torque performance. (a) Average torque. (b) Overload capability.

Fig.8 compares the flux density distribution of the proposed machines at a rated current of 7.8A and an overload current of 15A. The results indicate that only the split teeth exhibit partial saturation under both rated and overload conditions. It is noteworthy that the proposed machine does not exhibit any severe saturation under overload conditions. As a result, the torque production of the proposed machine remains unaffected

under overload conditions, and it demonstrates good linearity with an increase in input current. This remarkable overload capability can be attributed to the reduced non-working harmonics excited by armature winding.

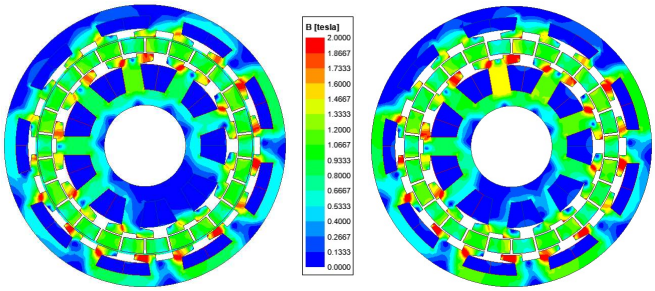

(a) (b)

Fig. 8. Flux density distribution of the proposed machine under different conditions. (a) Rated condition. (b) Overload condition.

B. Power Factor

Fig. 9 shows the input current and the fundamental harmonic of the induced voltages for both CWA-DSVM and the proposed DSVM under the rated condition. It can be observed that the angle difference (φ) between the current and induced voltage is not large in the proposed machine, with a value of 23.5 degrees. In contrast, a more evident angle difference can be observed in the CWA-DSVM, which is 38.7 degrees. As a result, the power factor ($\cos\varphi$) of the proposed machine is as high as 0.91, while the power factor of the CWA-DSVM is only 0.79. The high power factor of the proposed DSVM is mainly due to the adoption of the advanced winding design that effectively reduces non-working even-order harmonics. The reduction of those harmonics in the armature reaction results in a significant decrease in inductance, further contributing to the improvement of the power factor in the proposed machine.

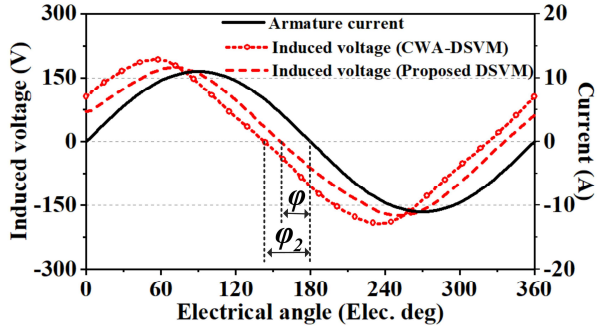

Fig. 9. Input current and the induced voltage.

Fig. 10 compares the power factors under different input currents of the CWA-DSVM and the proposed DSVM. The power factor continuously decreases with the increasing current. The value of the power factor of the proposed machine is over 0.7 under the overload condition (about two times the rated current). However, the value of the CWA-DSVM is decreased to about 0.5 under the same condition. Therefore, the proposed machine exhibits significant improvement in power factor, demonstrating the merit of the proposed winding arrangement.

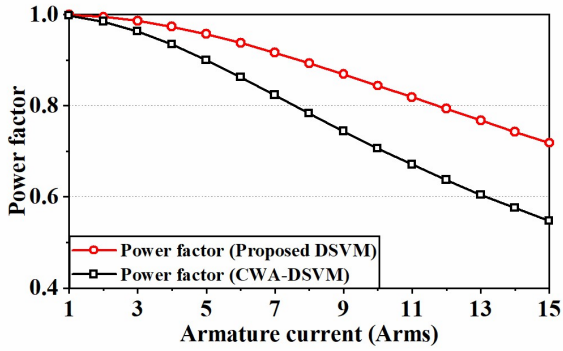

Fig. 10. Power factor under different input currents.

Table IV summarizes the electromagnetic performance of the proposed machine. It shows that the output torque is steady, with a low torque ripple of 0.61%. Additionally, the machine exhibits a relatively high power factor of 0.91, which is prominent in VMs. Furthermore, the proposed machine demonstrates a high efficiency of 91.1% considering copper loss, core loss, and PM eddy current loss, which are further investigated in Section V.

TABLE IV
PERFORMANCE OF THE PROPOSED DSVM

Items	Values
Rated torque	78.34 Nm
Rated power	2461 W
Phase back EMF	150.35 V
Torque ripple	0.61%
Power factor	0.91
Efficiency	91.1%

C. Unbalanced Magnetic Force

The unbalanced force acting on the rotor is mainly due to the asymmetric distribution of the magnetic field. The compensating structure can facilitate dual-stator machines to achieve a lower unbalanced force than single-stator machines. However, the inner and outer stator windings are always placed without any position difference in conventional dual-stator machines. Based on the conventional dual-stator machines, the proposed machine adopts a complementary stator structure and a special winding arrangement to reduce the unbalanced force.

Fig. 11 shows the flux distribution solely excited by armature windings of both conventional and proposed DSVMs. At this moment, i_a = 0A, i_b = -7.8A, and i_c = 7.8A. It can be seen from Fig. 11 (a) that the flux excited by the armature windings in the conventional machine is asymmetric and concentrated on the left-hand side. However, Fig. 11(b) shows that the asymmetrical displacement issue of phase windings of the conventional machine is well solved in the proposed DSVM. As shown in Fig. 11 (b), the flux distribution of the inner stator is concentrated on the right-hand side, which is opposite to the flux distribution of the outer stator. Thus, the proposed machine illustrates a more uniform flux distribution over the whole structure.

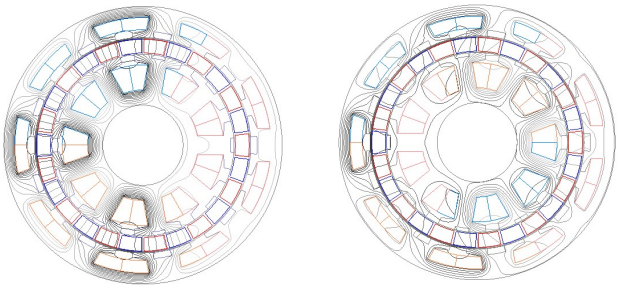

(a) (b)

Fig. 11. Flux distribution of machines. (a) CWA-DSVM (b) Proposed DSVM.

Fig. 12 further illustrates the effectiveness of the special winding arrangement in the proposed machine. As shown in Fig.12 (a), the unbalanced force of the rotor is analyzed under different excitations situations, including only inner stator winding, only outer stator winding, and both inner and outer stator windings, respectively. It is clear that the specially arranged inner stator winding can effectively reduce the magnetic force by counteracting a part of the force generated by the outer stator winding. Consequently, the radial unbalanced force can be notably reduced to 231N, which is 60.14% lower than the conventional machine, as shown in Fig. 12 (b).

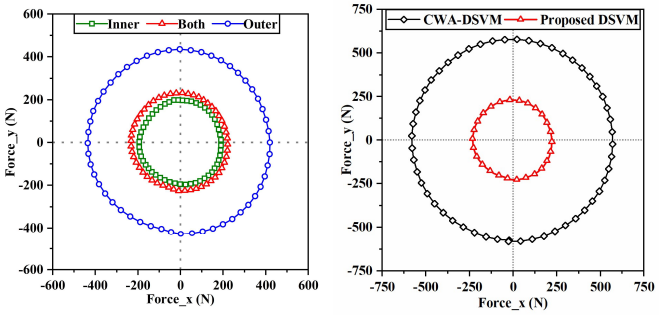

(a) (b)

Fig. 12. Unbalanced magnetic force. (a) Proposed DSVM under different excitation situations (b) CWA-DSVM and proposed DSVM.

IV. Mechanical Strength Verification

In this section, the stress analysis is conducted on the main rotor structural components of the DSVM to further validate the feasibility. The analysis results of the shaft are presented in Fig. 13. It can be found that the maximum equivalent stress on the rotor shaft occurred at the forefront of the bearing installation position. The maximum value is 102.9 MPa, which is well below the yield strength (210 GPa) of the shaft material (40Cr), confirming that the material is being used safely within its allowable stress range. The deformation of the shaft is also shown in Fig. 13(b), which is only 12.4 μm.

Due to the unique mounting design of the rotor assembly, the rotor shell used to place the PMs should be examined as well. Figures 14(a) and 14(b) show the maximum equivalent stress and deformation of the rotor shell, respectively. The maximum stress experienced by the shell is only 0.106 MPa, which is significantly lower than the yield strength of the steel (200 GPa). Additionally, the deformation of the shell is only 0.027 μm, which is negligible in comparison to the 1 mm air gap length.

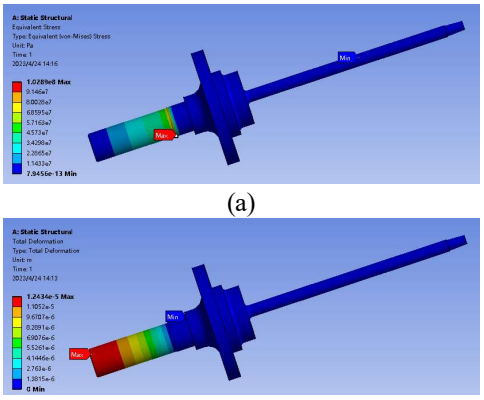

(a) (b)

Fig. 13. Mechanical analysis of rotor shaft. (a) Stress distribution. (b) Deformation distribution.

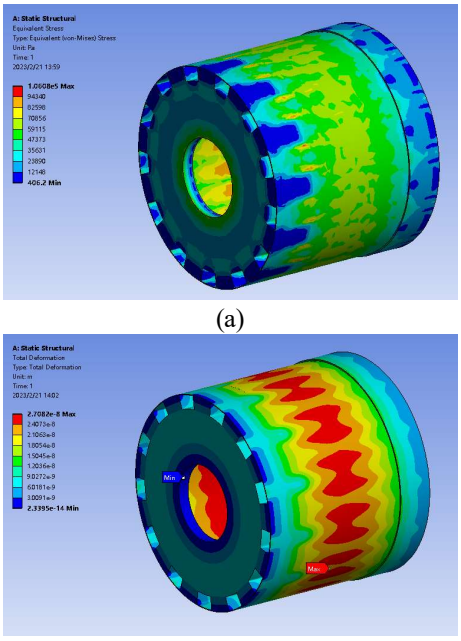

(a) (b)

Fig. 14. Mechanical analysis of rotor shell. (a) Stress distribution. (b) Deformation distribution.

V. Loss Analysis and Thermal Verification

The losses of the proposed DSVM are investigated, including copper loss, core loss, and PM eddy current loss. In this section, the major losses are calculated and treated as the thermal source to verify the temperature rise of the proposed machine. The calculation results are summarized in Table V under the rated condition.

TABLE V
Losses and Efficiency of the Proposed DSVM

Parameters	Values
Copper loss of outer stator winding	126 W
Copper loss of inner stator winding	83 W
Core loss of outer stator	8.6 W
Core loss of inner stator	7.6 W
PM eddy current loss	15 W
Total loss	240.2 W
Efficiency	91.1%

Fig. 15 shows the temperature distribution of the proposed machine under the rated condition with 25℃ ambient temperature. The cooling mode is natural cooling. Based on the result shown in Fig. 15(a), it is apparent that the inner stator winding experiences the highest average temperature among all components, reaching a maximum of 100.336℃, whereas the outer stator core exhibits the lowest average temperature of 86.27℃. Further detailed temperature distributions for each component can be observed in Figs. 15(b) to 15(f). Notably, the highest temperature of the proposed machine is 100.756℃, situated on the inner stator teeth that are near the inner stator winding, while the lowest temperature is found on the surface of the outer stator core at 85.35℃. As is typical of dual-stator machines, the inner stator components, including the stator core and winding, exhibit higher temperatures than the outer stator components. The average temperatures for the inner stator core, inner stator winding, outer stator core, and outer stator winding are 99.816℃, 100.336℃, 86.27℃, and 86.76℃, respectively.

In the proposed machine, the insulation grade is set to grade F, and the magnet material is selected as N38EH. The highest simulated temperature of the whole machine under rated conditions is found to be 100.756℃, which is below the allowable limit of grade F. Additionally, the rotor magnets experienced the highest temperature of 93.51℃. These results collectively confirm the safety and feasibility of the proposed machine for natural cooling.

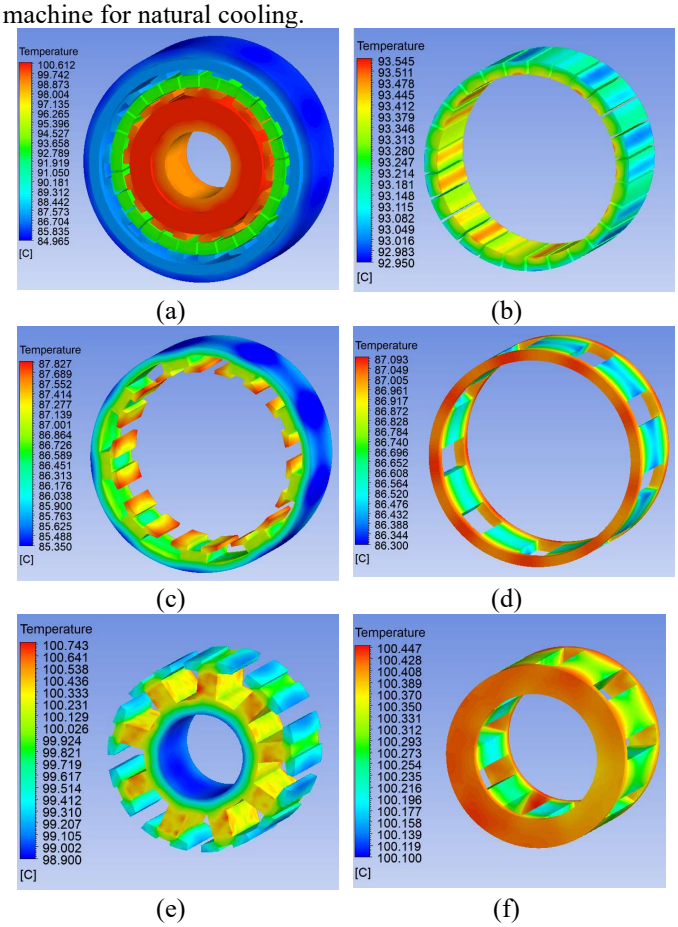

Fig. 15. Temperature distribution of the proposed DSVM. (a) The whole structure. (b) Rotor PM (c) Outer stator core. (d) Outer stator winding. (e) Inner stator core. (f) Inner stator winding.

VI. Experimental Verification

A prototype is fabricated and tested to validate the analysis and simulation results. Fig. 16 shows the prototype and its detailed structures. Both inner and outer stators are composed of laminations and double-layer concentrated windings, and the stator laminations are shown in Fig. 16 (a) and (b). The rotor is composed of PMs sandwiched between the two stators. Fig. 16 (c) presents a stainless-steel rotor shell, which is designed for locating the PM segments. The inner and outer stators are first fixed on the machine mountings when assembling the prototype, as shown in Fig. 16 (d). Then, the N magnets are inserted into the cavities in the rear end of the rotor shell, and the rotor shell is assembled to the stator assembly through the shaft. Subsequently, the S magnets are inserted into the cavities in the front end of the rotor shell. Fig. 16 (e) depicts a clear view of the assembling process of PMs. Finally, the assembled prototype with the machine shell is shown in Fig. 16 (f).

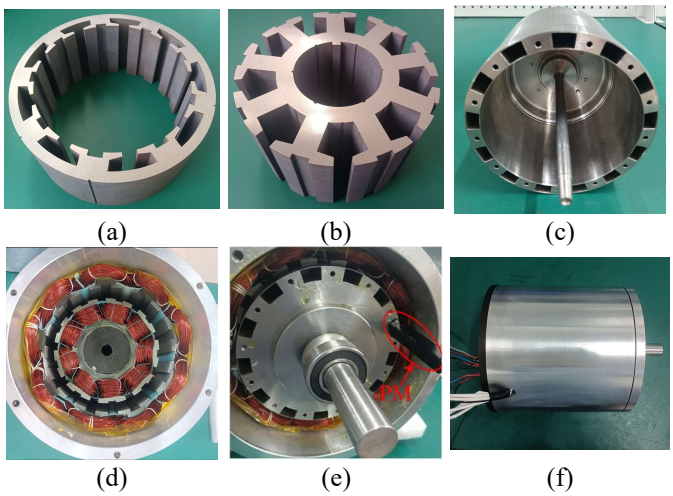

Fig. 16. Main components of the prototype. (a) Outer stator core. (b) Inner stator core. (c) Rotor shell. (d) Stator assembly. (e) Stator and rotor assembly. (f) Prototype.

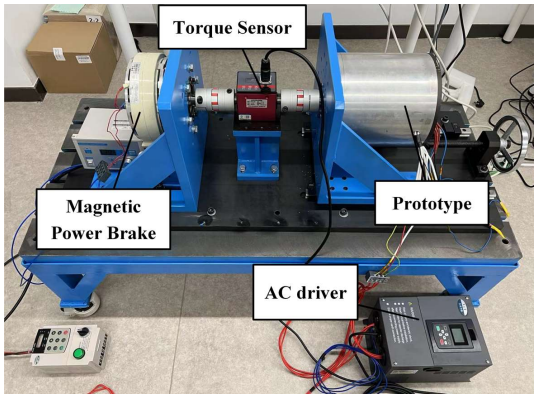

Fig. 17. The testing platform of the proposed DSVM.

Fig. 17 presents the setup for the testing platform, which utilizes a magnetic power brake as a load. The no-load back EMF is first measured at 300rpm to verify the performance of the proposed machine initially. The results, including the phase back-EMF waveform and the THD, are presented in Fig. 18. According to the simulation result in Fig. 18, the amplitude of the fundamental harmonic is 150.35V, while the experimental measurement recorded a value of 148.8V. It also can be seen in

Fig. 18(b) that the simulated THD value is 0.41%, while the experimental result is 1.05%, which is relatively close to the simulation result.

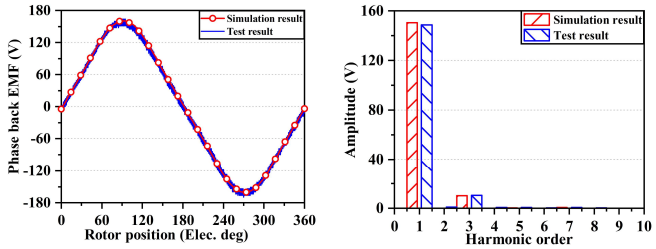

(a) (b)

Fig. 18. Comparison of simulated and tested phase back EMFs of the proposed DSVM. (a) Waveforms. (b) Harmonic spectra.

Fig. 19 depicts the waveform of the output torque, both simulated and tested, under a rated phase current of 7.8A. The test result is found to be well in agreement with the simulation result, but its magnitude is slightly lower. This is due to manufacturing tolerance, such as the lamination steel quality difference between the simulation model and the fabricated prototype. Fig. 20 shows the change in output torque as the current varies from 0A to 8A. The output torque linearly increases from 0Nm to 74.45Nm. The test results are then compared to the simulation ones. It can be found that the two curves are nearly identical.

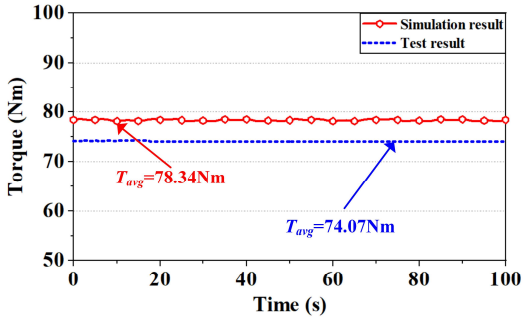

Fig. 19. Steady torque comparison of simulated and test results.

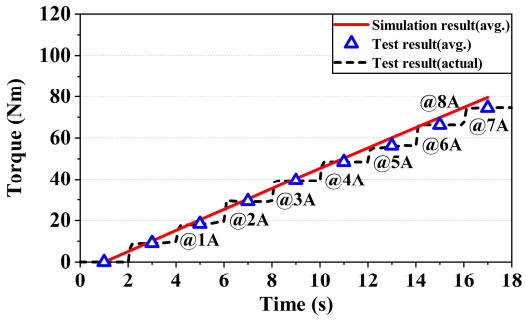

Fig. 20. Simulated and tested torque performance versus armature current.

Thermal issues are a constant challenge for dual-stator machines due to their specialized structure, with the inner stator being especially prone to heat buildup due to its poor heat dissipation properties. According to the simulation result, the temperature of the inner stator winding is indeed higher than the outer stator, which is 100°C. To ensure thermal safety, the temperature rise of the inner and outer stator windings is measured and verified. The proposed motor operates with natural cooling, and its temperature is measured through sensors located at the end of both inner and outer armature windings. Fig. 21 depicts the trend of temperature increase in the prototype under the rated condition. The temperature stabilizes after 100 minutes, and the temperature of the inner stator winding is found to be higher than that of the outer stator winding, which is consistent with the simulation result. It is noteworthy that, under the insulation grade F, the highest measured temperature is found to be below the maximum allowable temperature of 155°C. These findings confirm the safety and suitability of the proposed machine for natural cooling.

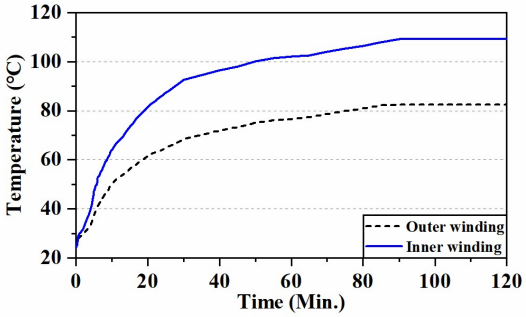

Fig. 21. Temperature of inner and outer windings.

VII. Conclusion

This paper presents a novel complementary DSVM with a high power factor and low unbalanced force. The electromagnetic design principle is analyzed, and mechanical structure and thermal field are comprehensively simulated. The results demonstrate that the proposed DSVM has outstanding electromagnetic performance compared to traditional DSVMs. By adopting a phase-shifted dual winding arrangement, the unbalanced force is significantly reduced by 60.14% while the power factor is notably improved to over 0.91. Additionally, the mechanical strength of the rotor assembly, which has been validated by using finite element analysis, guarantees efficient operation and reliable performance of the dual-stator machine. Moreover, the temperature rise distribution of the machine has been analyzed, with the highest temperature reaching 100.7°C, which is below the limit of insulation grade F and thus ensures a stable motor operation under the rated condition. The test results of the prototype align well with the simulation results and satisfy the requirements of various low-speed direct-drive applications in the industry.

Acknowledgment

This work was supported by the Research Grant Council of the Hong Kong Government under Project PolyU 152109/20E.

References

[1] C. Lee, "Vernier motor and its design," *IEEE Trans. on Power Apparatus and Syst.*, vol. 82, no. 66, pp. 343–349, Jun. 1963.
[2] E. P. Wigner, "Theory of traveling-wave optical laser," *Phys. Rev.*, vol. 134, pp. A635–A646, Dec. 1965.
[3] A. Ishizaki, "Theory and optimum design of PM Vernier motor," *in Seventh International Conference on Electrical Machines and Drives*, Durham, UK, 1995, vol. 1995, pp. 208–212.
[4] T. A. Lipo and A. Toba, "Generic torque-maximizing design methodology of surface permanent-magnet Vernier machine," *IEEE Trans. on Ind. Applicat.*, vol. 36, no. 6, pp. 1539–1546, Dec. 2000.

[5] D. Li, T. Zou, R. Qu, and D. Jiang, "Analysis of fractional-slot concentrated winding PM Vernier machines with regular open-slot stators," *IEEE Trans. on Ind. Applicat.*, vol. 54, no. 2, pp. 1320–1330, Mar. 2018.

[6] B. Kim and T. A. Lipo, "Operation and design principles of a PM Vernier motor," *IEEE Trans. on Ind. Applicat.*, vol. 50, no. 6, pp. 3656–3663, Nov. 2014.

[7] J. Yang et al., "Quantitative comparison for fractional-slot concentrated-winding configurations of permanent-magnet Vernier machines," *IEEE Trans. Magn.*, vol. 49, no. 7, pp. 3826–3829, Jul. 2013.

[8] K. Okada, N. Niguchi, and K. Hirata, "Analysis of a Vernier motor with concentrated windings," *IEEE Trans. Magn.*, vol. 49, no. 5, pp. 2241–2244, May 2013.

[9] T. Zou, D. Li, R. Qu, D. Jiang, and J. Li, "Advanced high torque density PM Vernier machine with multiple working harmonics," *IEEE Trans. on Ind. Applicat.*, vol. 53, no. 6, pp. 5295–5304, Nov. 2017.

[10] D. Li, R. Qu, J. Li, and W. Xu, "Consequent-pole toroidal-winding outer-rotor Vernier permanent-magnet machines," *IEEE Trans. on Ind. Applicat.*, vol. 51, no. 6, pp. 4470–4481, Nov. 2015.

[11] A. Toba and T. A. Lipo, "Novel dual-excitation permanent magnet Vernier machine," *Conference Record of the 1999 IEEE Industry Applications Conference*. Thirty-Forth IAS Annual Meeting (Cat. No.99CH36370), Phoenix, AZ, USA, 1999, pp. 2539-2544 vol.4.

[12] D. Li, R. Qu, W. Xu, J. Li, and T. A. Lipo, "Design procedure of dual-stator spoke-array Vernier permanent-magnet machines," *IEEE Trans. on Ind. Applicat.*, vol. 51, no. 4, pp. 2972–2983, Jul. 2015.

[13] Z. Song, C. Liu, and H. Zhao, "Quantitative comparison of distinct dual-stator permanent magnet Vernier machines for direct-drive applications," *IEEE Trans. Magn.*, vol. 55, no. 7, pp. 1–6, Jul. 2019.

[14] D. Li, R. Qu, and Z. Zhu, "Comparison of Halbach and dual-side Vernier permanent magnet machines," *IEEE Trans. Magn.*, vol. 50, no. 2, pp. 801–804, Feb. 2014.

[15] H. Wang, S. Fang, X. Lu, H. Ni, H. Yang, and H. Lin, "Analysis of a new dual-stator Vernier machine with hybrid magnet flux-reversal arrangement," *IEEE Trans. Appl. Supercond.*, vol. 29, no. 2, pp. 1–5, Mar. 2019.

[16] Z. S. Du and T. A. Lipo, "Design of an improved dual-stator ferrite magnet Vernier machine to replace an industrial rare-earth IPM machine," *IEEE Trans. Energy Convers.*, vol. 34, no. 4, pp. 2062–2069, Dec. 2019.

[17] M. Raza, W. Zhao, T. A. Lipo, and B. Kwon, "Performance comparison of dual airgap and single airgap spoke-type permanent-magnet Vernier machines," *IEEE Trans. Magn.*, vol. 53, no. 6, pp. 1–4, Jun. 2017.

[18] D. Li, R. Qu, and T. A. Lipo, "High-power-factor Vernier permanent-magnet machines," *IEEE Trans. on Ind. Applicat.*, vol. 50, no. 6, pp. 3664–3674, Nov. 2014.

[19] L. Wu and R. Qu, "A novel dual-stator Vernier permanent magnet machine with improved power factor," *IEEE Trans. on Ind. Applicat*., vol. 58, no. 3, pp. 3486–3496, May 2022.

[20] H. Gorginpour, "Dual‐stator consequent‐pole Vernier PM motor with improved power factor," *IET Electric Power Applications*, vol. 13, no. 5, pp. 652–661, May 2019.

[21] Y. Shi and T. W. Ching, "Power factor analysis of dual-stator permanent magnet Vernier motor with consideration on turn-number assignment of inner and outer stator windings," *IEEE Trans. Magn.*, vol. 57, no. 2, pp. 1–5, Feb. 2021.

[22] Y. Chen, W. Fu, and X. Weng, "A concept of general flux-modulated electric machines based on a unified theory and its application to developing a novel doubly-fed dual-stator motor," *IEEE Trans. Ind. Electron.*, vol. 64, no. 12, pp. 9914–9923, Dec. 2017.

[23] T. W. Ching, K. T. Chau and W. Li, "Power factor improvement of a linear Vernier permanent-magnet machine using auxiliary DC field excitation," *IEEE Trans. Magn.*, vol. 52, no. 7, pp. 1-4, Jul. 2016.

[24] M. Cheng, P. Han, Y. Du and H. H. Wen, General Airgap Field Modulation Theory for Electrical Machines and Its Applications. Beijing:China Machine Press,2021.

[25] Z. Q. Zhu, D. Ishak, D. Howe, and J. Chen, "Unbalanced magnetic forces in permanent-magnet brushless machines with diametrically asymmetric phase windings," *IEEE Trans. on Ind. Applicat.*, vol. 43, no. 6, pp. 1544–1553, 2007.

Jiahui Huang received the B.Sc. degree in electrical engineering and automation from Xiamen University of Technology, China, in 2013, and the M.Sc. degree in electrical engineering from the Hong Kong Polytechnic University, Hong Kong, in 2015, where she is currently pursuing the Ph.D. degree in electrical engineering. Her main research interests include the design, analysis, and optimization of electric machines.

W. N. Fu obtained his Ph.D. from The Hong Kong Polytechnic University (PolyU) in 1999. He is a Professor at Shenzhen Institutes of Advanced Technology. He worked at PolyU about 13 years as an Associate Professor and Full Professor. He was one of the key developers at Ansoft Corporation in Pittsburgh, USA. He has about seven years of working experience at Ansoft, focusing on the development of commercial software Maxwell. Prof. Fu has made many contributions to the theory and application of electromagnetic field computation and electric device design, including the publication of over 250 refereed journal papers. Prof. Fu's research interests mainly focus on computational electromagnetics, optimal design of electric devices, applied electromagnetics, and novel electric machines.

Shuangxia Niu (Senior Member, IEEE) received the B.Sc. and M.Sc. degrees from Tianjin University, Tianjin, China, in 2002 and 2005, respectively, and the Ph.D. degree from the University of Hong Kong, Hong Kong, SAR, China, in 2009, all in electrical engineering. She is currently a professor with the Department of Electrical and Electronic Engineering, The Hong Kong Polytechnic University. She authored or coauthored more than 100 papers in leading journals. Prof. Niu is currently an Associate Editor for the IEEE Journal of Emerging and Selected Topics in Power Electronics.

Xing Zhao (Member, IEEE) received the B.Eng. degree from Nanjing University of Aeronautics and Astronautics, China, in 2014, and the Ph.D. degree from The Hong Kong Polytechnic University, Hong Kong SAR, in 2020, both in Electrical Engineering. Between Aug. 2020 and Oct. 2021, he served as a Research Assistant Professor with the Department of Electrical Engineering, The Hong Kong Polytechnic University. From Jul. 2019 to Jan. 2020, he was a Visiting Scholar with the Center for Advanced Power Systems, Florida State University, Tallahassee, USA. Currently, he is a Lecturer in the School of Physics, Engineering and Technology, University of York, UK. He has authored 75 technical papers in the international journals and conferences. His research interests include advanced electrical machines and power electronics for electric vehicles and renewable energy systems. He is an Associate Editor for IEEE Trans. Transportation Electrification, IEEE Trans. Energy Conversion, and IEEE Open Journal of the Industrial Electronics Society.